Volume 27
Number 31
21 August 2025
Pages 5215–5364

CrystEngComm

rsc.li/crystengcomm

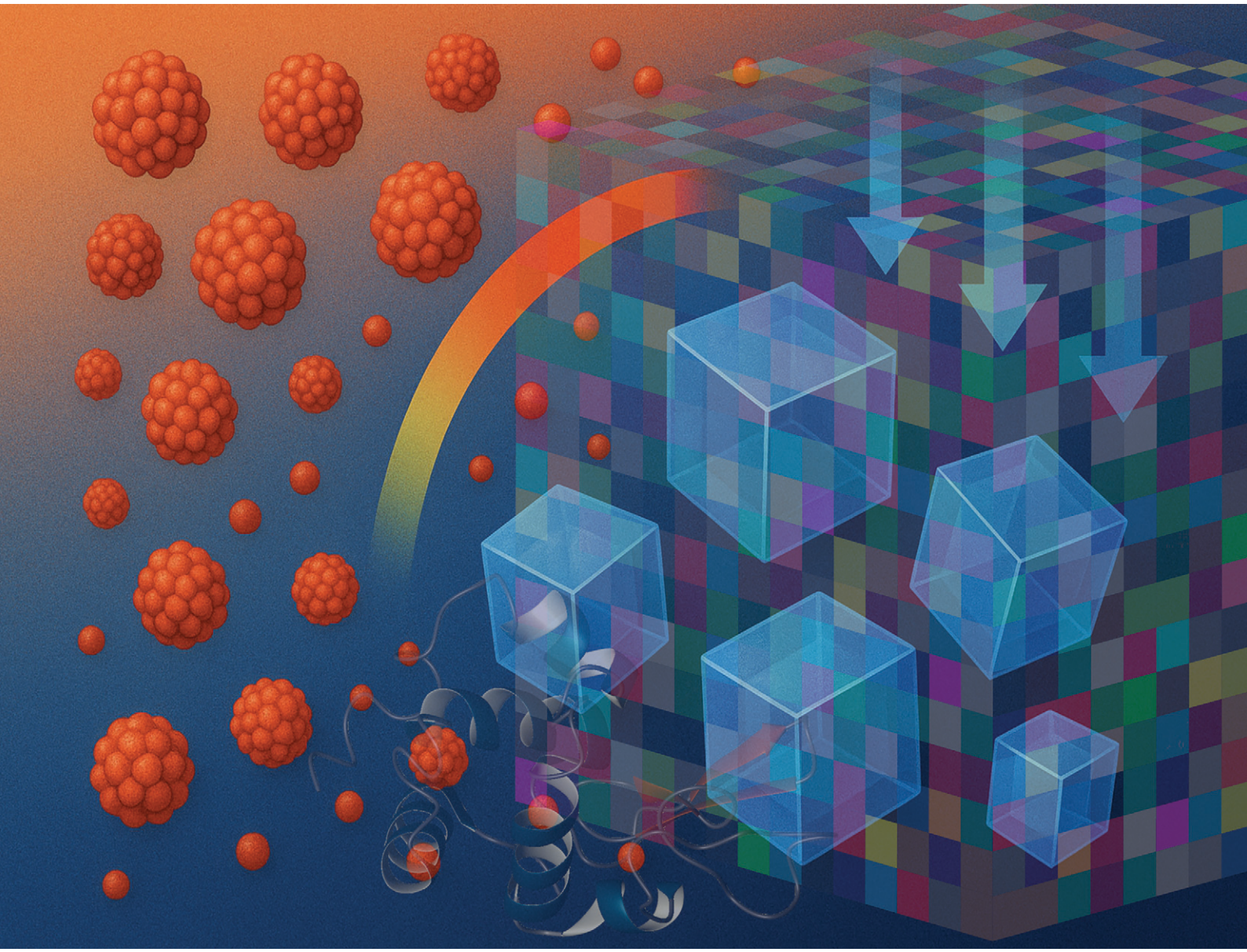

ISSN 1466-8033

ROYAL SOCIETY OF CHEMISTRY

COMMUNICATION

Mayank Vashishtha and K. Vasanth Kumar
Nucleation rate and Gibbs free energy of nucleation of APIs, large molecule, amino acid and inorganic materials in solution at different cooling rates

CrystEngComm

COMMUNICATION

View Article Online
View Journal | View Issue

Cite this: *CrystEngComm*, 2025, **27**, 5265

Received 5th May 2025,
Accepted 16th July 2025

DOI: 10.1039/d5ce00467e

rsc.li/crystengcomm

Nucleation rate and Gibbs free energy of nucleation of APIs, large molecule, amino acid and inorganic materials in solution at different cooling rates†

Mayank Vashishtha[a] and K. Vasanth Kumar *[b]

We propose a new mathematical model based on the classical nucleation theory to predict the nucleation rate, kinetic constant, and Gibbs free energy of nucleation using metastable zone width (MSZW) data as a function of solubility temperature. Unlike widely used models by Nývlt, Kubota, and Sangwal, which are limited in capturing the impact of varying cooling rates, the proposed model allows direct estimation of nucleation rates from MSZW data obtained under different cooling conditions. This is particularly advantageous for continuous or semi-batch crystallisation design, where cooling rate is a critical variable. The model has been successfully validated using experimental data from 22 solute–solvent systems, including 10 APIs, one API intermediate, lysozyme, and glycine, as well as 8 inorganic compounds. Predicted nucleation rates span from 10^{20} to 10^{24} molecules per m^3 s for APIs, and up to 10^{34} molecules per m^3 s for lysozyme, the largest molecule studied. Gibbs free energy of nucleation varies from 4 to 49 kJ mol^{-1} for most compounds, reaching 87 kJ mol^{-1} for lysozyme. The model also enables accurate prediction of induction time and key thermodynamic parameters such as surface free energy, critical nucleus size, and number of unit cells—based solely on MSZW data obtained at different cooling rates.

In this communication, we propose a useful mathematical model to predict the nucleation rate and Gibbs free energy of nucleation from metastable zone width (MSZW) values measured at different cooling rates. The model is validated using a broad dataset comprising 11 different active pharmaceutical ingredients (APIs)/solvent combinations involving 10 active pharmaceutical ingredients (APIs), 8 inorganic compound–solvent systems, one API intermediate, one amino acid, and one large molecule. The MSZW is crucial in crystallization processes because it defines the range of supersaturation where no spontaneous nucleation occurs, but crystal growth is possible.[1–4] MSZW helps to determine the precise supersaturation levels to avoid spontaneous nucleation, which can lead to undesirable crystal sizes or polymorphs.[5–7] Operating within the MSZW allows controlled crystal growth, ensuring consistent size and quality of the crystals. On the theoretical side, MSZW allows to calculate the nucleation rate which is a key factor in understanding and optimising the crystallisation.[5] Theoretically the nucleation rate is obtained using the MSZW measured at different cooling rates using theoretical models that includes the one developed by Nývlt,[8] Sangwal,[9] and Kubota.[1] These models allow to theoretically calculate the nucleation rate kinetic constant and the order of nucleation.[1,8–21] Moreover, these models relate the MSZW obtained at fixed saturation temperature with the rate of cooling. It will be useful to develop a theoretical model that can theoretically determine the nucleation rate at different cooling rates. Thus, to complement the established model of Nývlt, Sangwal and Kubota, we present a new mathematical model based on the classical nucleation theory that allows to calculate nucleation rate at different cooling rates using the MSZW data collected from different solubility onset temperature. Unlike existing models, which do not explicitly account for cooling rate, our approach directly incorporates its influence, enabling accurate prediction of nucleation rates across varying cooling conditions. Furthermore, as the model rely on the classical nucleation theory, it immediately allows to theoretically calculate the Gibbs free energy of nucleation as a function of temperature and supersaturation at the point of nucleation. From the Gibbs free energy, it is possible to calculate the surface free energy or the interfacial tension and the radius of the critical nucleus as a function of the operating variables that mainly include the supersaturation and the temperature at which the nucleation is observed. To demonstrate the

[a] *Department of Chemical Sciences, Synthesis and Solid State Pharmaceutical Centre, Bernal Research Institute, University of Limerick, Limerick V94 T9PX, Ireland*
[b] *Department of Chemical and Process Engineering, Faculty of Engineering and Physical Sciences, University of Surrey, Guildford GU2 7XH, UK.*
E-mail: v.kannuchamy@surrey.ac.uk

† Electronic supplementary information (ESI) available. See DOI: https://doi.org/10.1039/d5ce00467e

usefulness and universality of the proposed model, it was applied to experimental MSZW data from 22 different solute–solvent combinations. This dataset includes 10 different APIs across 11 API–solvent systems, eight inorganic compound–solvent combinations, as well as one API intermediate (L-arabinose), one amino acid (glycine), and one large biomolecule (lysozyme). The MSZW data, reported at different cooling rates, were used to extract key nucleation parameters, including the nucleation rate kinetic constant, Gibbs free energy of nucleation (ΔG), surface energy, and the critical nucleus radius, all evaluated as functions of supersaturation and nucleation temperature.

The metastable zone widths (MSZW) of solutions containing these single-component compounds, experimentally measured using the polythermal method, were obtained from the literature.[22–32] This method involves changing the temperature of the solution from a reference solubility temperature T^*_{ref} at a predefined cooling rate and detecting the onset of nucleation at T_{nuc}.[9] The relationship between the reference solution temperature, temperature at which nucleation can be observed or detected is shown in Fig. 1. In Fig. 1, we also showed the line of supersolubility concentration, solubility concentration and their relationship with the MSZW, ΔT_{max} and the supersaturation at the MSZW, ΔC_{max}.

According to the classical nucleation theory, the nucleation rate is defined as

$$J = k_n \exp(-\Delta G/RT) \quad (1)$$

During the cooling the crystallization, the undersaturated solution will be cooled from approximately T^*_{ref} + 5 °C at a fixed cooling rate of dT^*/dt until the nucleation or the phase change is observed or can be experimentally detected measured in the solution. The temperature where the nucleation is observed is T_{nuc}. So, at the point of nucleation, $T = T_{nuc}$ and thus eqn (1) becomes:

$$J = k_n \exp(-\Delta G/RT_{nuc}) \quad (2)$$

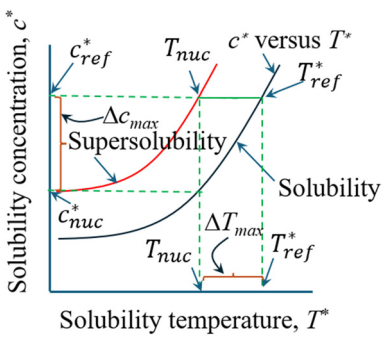

Fig. 1 The relationship between solubility concentration, c^* and solubility temperature, T^*. Also shown in the figures are the different parameters that can be experimentally fixed or obtained and their relationship between the MSZW (or $\Delta T_{max} = T^*_{ref} - T_{nuc}$) and the supersaturation (or $\Delta c_{max} = c^*_{ref} - c^*_{nuc}$) at the MSZW.

The nucleation rate can be defined in terms of cooling rate, $R' = \frac{dT^*}{dt}$ and the slope of solubility curve $\frac{dc^*}{dT^*}$ as follows

$$J = R' \frac{dc^*}{dT^*} \quad (3)$$

From eqn (2) and (3), it is possible to write that

$$k_n \cdot \exp(-\Delta G/RT_{nuc}) = R' \cdot \frac{dc^*}{dT^*} \quad (4)$$

At the point of nucleation,

$$\frac{dc^*}{dT^*} = \frac{\Delta c_{max}}{\Delta T_{max}} = \frac{c^*_{ref} - c^*_{nuc}}{T^*_{ref} - T_{nuc}} \quad (5)$$

where, $\Delta T_{max} = T^*_{ref} - T^*_{nuc}$ is the MSZW and Δc_{max} is the supersaturation (or the driving force required for crystallization) achieved at T_{nuc}, where primary nucleation is most likely to occur. The relationship between the solubility concentration c^* and the parameters that include T^*, T^*_{ref}, T_{nuc}, and MSZW (*i.e.*, ΔT_{max}) and the supersaturation concentration at ΔT_{max} (*i.e.*, Δc_{max}) are given in Fig. 1.

Substituting eqn (5) in (4), we get

$$k_n \exp(-\Delta G/RT_{nuc}) = R' \frac{\Delta c_{max}}{\Delta T_{max}} \quad (6)$$

Eqn (6) can be linearized as follows:

$$\ln\left(\frac{\Delta c_{max}}{\Delta T_{max}}\right) + \ln R' = \ln(k_n) - \frac{\Delta G}{RT_{nuc}} \quad (7)$$

From eqn (7), it is immediately evident that the model explicitly incorporates the cooling rate, along with the metastable zone width (ΔT_{max}), supersaturation at ΔT_{max}, and the nucleation temperature, to predict the nucleation rate constant (k_n) and related parameters under varying experimental conditions. Importantly, eqn (7) establishes a direct link between key nucleation parameters such as the nucleation rate constant (k_n), Gibbs free energy of nucleation (ΔG), and induction time (as later shown in eqn (12)) and experimentally measurable quantities. Theoretically, a plot of $\ln(\Delta C_{max}/\Delta T_{max})$ *versus* $1/T_{nuc}$ should be linear with a negative slope whose value will be equal to $\Delta G/R$ with an intercept equal to $\ln(k_n)$. Once the nucleation kinetic constant, k_n and the ΔG is determined, then mathematically it is possible to estimate at the nucleation rate J using eqn (2) at a fixed cooling rate R' and the MSZW measured at different T^*_{ref} (and the corresponding T_{nuc}). Furthermore, from the classical nucleation theory, it is also possible to calculate the surface energy, or the interfacial tension associated with the formation of stable nucleus using the expression:[9]

$$\frac{\Delta G}{RT_{nuc}} = \frac{16\pi\gamma^3 \vartheta^2}{3R^2 T^2_{nuc} (\ln S)^2} \frac{1}{RT_{nuc}} \quad (8)$$

Once the surface energy is calculated using eqn (8), we can mathematically calculate the radius of the critical nucleus using the expression:[9]

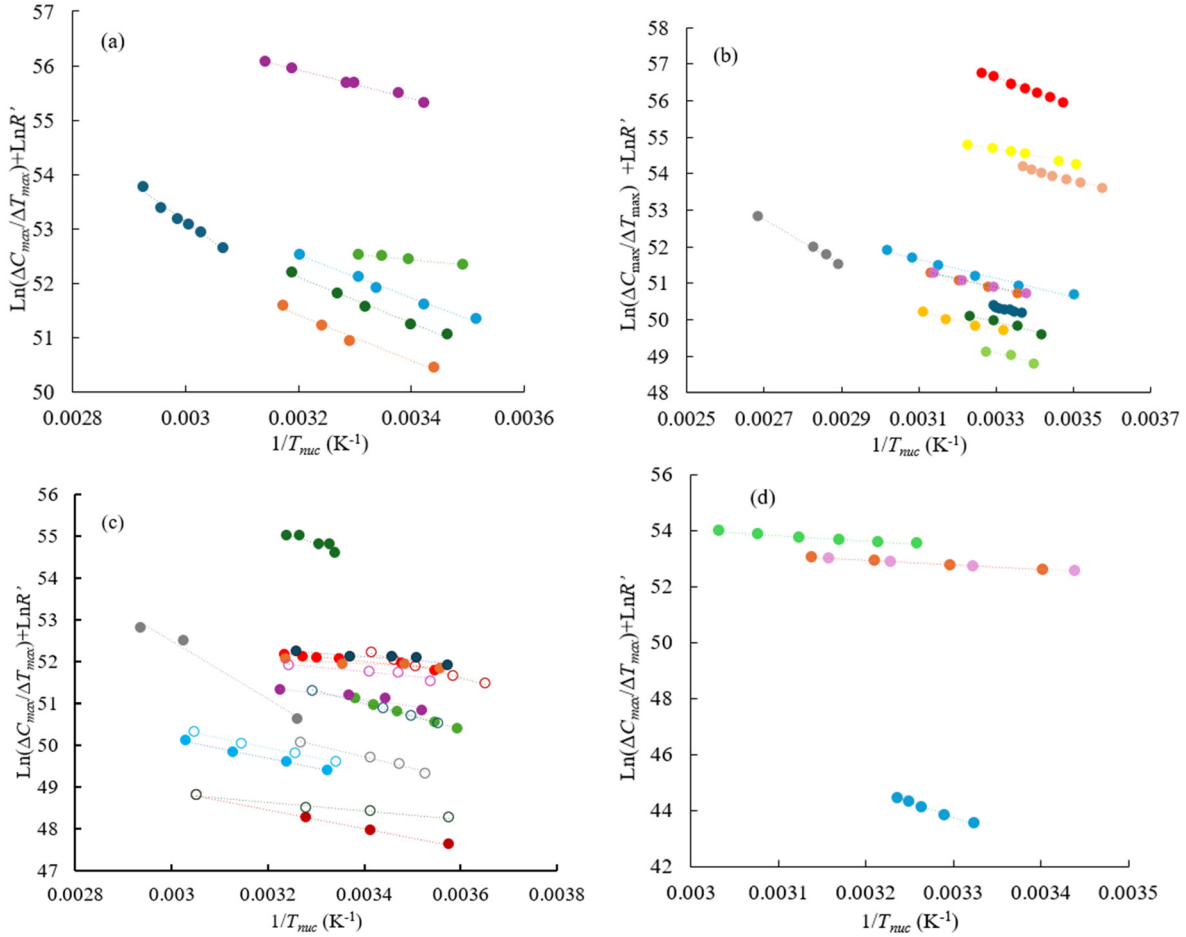

Fig. 2 Plot of $\ln(\Delta C_{max}/\Delta T_{max}) + \ln(R')$ *versus* $1/T_{nuc}$ for (a) 6 different combinations of API and solvents involving 4 APIs, (b) 11 different combinations of API and solvents involving 6 APIs, (c) combination of inorganics/solvents involving 8 different compounds and (d) API intermediate, amino acid and a large molecule. Note: these values are valid only at the cooling rates studied given in Table 1. Fig. 2a: ●: paracetamol/water (R': 0.5 K s^{-1}); ●: dextrose/water (R': 0.0278 K s^{-1}); ●: L-asparagine monohydrate/water (R': 0.005 K s^{-1}); ●: L-asparagine monohydrate/water (R': 0.0033 K s^{-1}). Fig. 2b: ●: ibuprofen/ethanol (R': 0.0167 K s^{-1}); ●: paracetamol/ethanol (R': 0.0167 K s^{-1}); ●: pyrazinamide/acetone (R': 0.0167 K s^{-1}); ●: fenofibrate/ethyl acetate (R': 0.05 K s^{-1}); ●: gestodene/ethanol (R': 0.0083 K s^{-1}); ●: gestodene/ethanol (R': 0.005 K s^{-1}); ●: carbamazepine_saccharine/ethanol (R': 0.0167 K s^{-1}); ●: pyrazinamide/acetone (R': 0.0033 K s^{-1}); ●: gestodene/ethanol (R': 0.00167 K s^{-1}). Fig. 2c: ●: $NaNO_3$/NaCl + $NaNO_3$ + H_2O solution (R': 0.000833 K s^{-1}); ●: $NaNO_3$/NaCl + $NaNO_3$ + H_2O solution (R': 0.001667 K s^{-1}); ●: $CoSO_4$/water (R': 0.000833 K s^{-1}); ○: $CoSO_4$/water (R': 0.001667 K s^{-1}); ●: $CoSO_4$/water (R': 0.0025 K s^{-1}); ○: $(NH_4)_2B_4O_7{\cdot}4H_2O$/water ($R'$: 0.00833 K s^{-1}); ○: $(NH_4)_2B_4O_7{\cdot}4H_2O$/water ($R'$: 0.0025 K s^{-1}); ●: Na_3VO_4/NaOH solution (R': 0.005 K s^{-1}); ●: $Sr(OH)_2{\cdot}8H_2O$/water (R': 0.001388 K s^{-1}); ○: $Sr(OH)_2{\cdot}8H_2O$/water (R': 0.00277 K s^{-1}); ●: ZnL_2/water (R': 0.00138 K s^{-1}); ○: ZnL_2/water (R': 0.00275 K s^{-1}); ●: borax/water (R': 0.003472 K s^{-1}); ○: borax/water (R': 0.01066 K s^{-1}); ●: ammonium oxalate/water (R': 0.000833 K s^{-1} – plotted in secondary axis). Fig. 2d: ●: L-arabinose/water (R': 0.0083 K s^{-1}); ●: glycine/water (R': 0.001667 K s^{-1}); ●: glycine/water (R': 0.005 K s^{-1}); ●: lysozyme/NaCl solution (R': 0.002778 K s^{-1} – we assumed this cooling rate – shown in secondary axis).

$$r_c = \frac{2\gamma\vartheta}{kT_{nuc}\ln S} \quad (9)$$

In Fig. 2a and b, we showed the plot of $\ln(\Delta C_{max}/\Delta T_{max})$ *versus* $1/T_{nuc}$ for 11 different combinations of APIs and solvents. In Fig. 2c and d we showed the plot of $\ln(\Delta C_{max}/\Delta T_{max})$ *versus* $1/T_{nuc}$ for 8 combinations of inorganic compounds and solvents, as well as for one API intermediate (L-arabinose), one amino acid (glycine) and a large biomolecule (lysozyme). The ΔC_{max}, ΔT_{max}, and the corresponding nucleation temperature during the crystallization of these different compounds from their solution and the solvents involved are given in Table 1. All the experimental values were obtained from literature (see Table 1). From Fig. 2, it is evident that the proposed model provides an excellent fit to the experimental data across all systems studied, regardless of the nature of the solutes (APIs, inorganic compounds, or biomolecules), the solvents used, or the specific experimental conditions, including the studied cooling rates. From Fig. 2 and using eqn (7) we calculated the nucleation rate kinetic constant, k_n and the Gibbs free energy of nucleation, ΔG. The calculated k_n, ΔG and the corresponding r^2 values are given in Table 1. In most cases the coefficient of determination was always greater than 0.97, indicating the proposed model provides an excellent representation of the experimental data across systems

Table 1 Nucleation parameters as a function of cooling rate obtained using the proposed model as in eqn (7) for 11 different combinations of APIs/solvents that involve 10 APIs, 8 inorganic compounds in their solution, an API intermediate, amino acid and lysozyme (a large molecule)

API/solvent	R', K s^{-1}	k_n, m^{-3} s^{-1}	T_{nuc}, K	$S = c^*_{nuc}/c^*_{ref}$	Δc_{max}, molecules per m^3	ΔT_{max}, K	ΔG, kJ mol^{-1}	J, m^{-3} s^{-1}	γ, mJ m^{-2}	r_c, m	$V_{cell}^{1/3}$, m	$\lambda = 2r_c/V_{cell}^{1/3}$	N_m/V	t_{ind}, s	r^2	Ref.
Psilocybin/water	0.0167	6.4×10^{32}	326.02	3.86	6.6×10^{25}	14.87	62.1	7.12×10^{22}	28.35	9.32×10^{-10}	1.38×10^{-9}	1.35	6.35×10^{25}	892	0.9789	23
			330.35	3.13	7.2×10^{25}	12.38		9.63×10^{22}	25.55	9.82×10^{-10}		1.42	7.15×10^{25}	743		
			332.70	2.83	7.63×10^{25}	11.38		1.13×10^{23}	24.13	1.01×10^{-9}		1.46	7.71×10^{25}	683		
			334.91	2.61	8.17×10^{25}	11.01		1.3×10^{23}	22.98	1.04×10^{-9}		1.50	8.65×10^{25}	661		
			338.30	2.21	8.31×10^{25}	9.01		1.64×10^{23}	20.39	1.10×10^{-9}		1.59	8.85×10^{25}	541		
			341.90	1.87	8.2×10^{25}	6.09		2.06×10^{23}	17.52	1.19×10^{-9}		1.72	7.55×10^{25}	366		
Paracetamol/ethanol	0.0167	2.3×10^{26}	285.21	1.59	5.14×10^{26}	22.99	15.22	3.75×10^{23}	7.97	8.70×10^{-10}	1.14×10^{-9}	1.51	5.17×10^{26}	1379	0.9823	23
			288.86	1.54	5.13×10^{26}	21.05		4.06×10^{23}	7.63	8.90×10^{-10}		1.54	5.14×10^{26}	1263		
			296.63	1.38	4.72×10^{26}	15.61		4.80×10^{23}	6.42	9.70×10^{-10}		1.68	4.50×10^{26}	937		
			299.74	1.41	5.2×10^{26}	16.85		5.11×10^{23}	6.75	9.46×10^{-10}		1.64	5.18×10^{26}	1011		
			303.93	1.41	5.72×10^{26}	16.70		5.56×10^{23}	6.81	9.41×10^{-10}		1.63	5.58×10^{26}	1002		
			304.63	1.49	6.56×10^{26}	19.73		5.64×10^{23}	7.55	8.94×10^{-10}		1.55	6.68×10^{26}	1184		
			310.22	1.54	7.76×10^{26}	21.05		6.29×10^{23}	8.00	8.69×10^{-10}		1.50	7.95×10^{26}	1263		
Pyrazinamide/acetone	0.0016	1.7×10^{25}	294.45	1.10	3.5×10^{24}	3.68	22.63	1.64×10^{21}	3.31	1.65×10^{-9}	8.30×10^{-10}	3.97	3.62×10^{24}	2210	0.9007	30
			299.72	1.11	4.4×10^{24}	3.60		1.92×10^{21}	3.42	1.62×10^{-9}		3.9	4.17×10^{24}	2162		
			305.51	1.07	3.85×10^{24}	2.89		2.29×10^{21}	2.75	1.81×10^{-9}		4.36	3.97×10^{24}	1734		
			311.14	1.05	2.97×10^{24}	2.26		2.69×10^{21}	2.05	2.09×10^{-9}		5.05	3.65×10^{24}	1354		
Pyrazinamide/acetone	0.0033	2.4×10^{25}	292.70	1.18	5.67×10^{24}	5.43	21.42	3.62×10^{21}	4.56	1.37×10^{-9}	8.30×10^{-10}	3.29	5.90×10^{24}	1628	0.9602	30
			298.10	1.18	6.93×10^{24}	5.23		4.25×10^{21}	4.59	1.36×10^{-9}		3.28	6.67×10^{24}	1568		
			303.73	1.15	7.24×10^{24}	4.67		4.99×10^{21}	4.19	1.43×10^{-9}		3.43	7.00×10^{24}	1402		
			309.84	1.10	6.08×10^{24}	3.56		5.89×10^{21}	3.28	1.61×10^{-9}		3.88	6.31×10^{24}	1069		
L-Asparagine monohydrate/water	0.0016	1.3×10^{28}	290.65	1.27	2.16×10^{25}	4.40	34.69	7.81×10^{21}	6.79	1.42×10^{-9}	8.67×10^{-10}	3.28	2.06×10^{25}	2639	0.9723	24
			297.87	1.26	2.92×10^{25}	5.11		1.11×10^{22}	6.75	1.43×10^{-9}		3.29	3.39×10^{25}	3068		
			303.94	1.22	3.22×10^{25}	4.05		1.46×10^{22}	6.13	1.50×10^{-9}		3.46	3.56×10^{25}	2433		
			308.46	1.20	3.68×10^{25}	3.50		1.78×10^{22}	5.90	1.53×10^{-9}		3.52	3.76×10^{25}	2098		
			315.24	1.17	4.24×10^{25}	2.76		2.39×10^{22}	5.38	1.60×10^{-9}		3.69	3.96×10^{25}	1654		
L-Asparagine monohydrate/water	0.0033	2.5×10^{28}	288.69	1.39	2.88×10^{25}	6.36	34.55	1.42×10^{22}	8.38	1.28×10^{-9}	8.67×10^{-10}	2.95	2.71×10^{25}	1907	0.9887	24
			294.24	1.49	4.67×10^{25}	8.74		1.86×10^{22}	9.66	1.19×10^{-9}		2.75	4.88×10^{25}	2622		
			301.39	1.37	4.90×10^{25}	6.60		2.6×10^{22}	8.36	1.28×10^{-9}		2.95	5.15×10^{25}	1980		
			305.81	1.36	5.83×10^{25}	6.15		3.17×10^{22}	8.28	1.29×10^{-9}		2.97	5.86×10^{25}	1844		
			313.68	1.26	6.02×10^{25}	4.32		4.46×10^{22}	6.92	1.41×10^{-9}		3.25	5.79×10^{25}	1295		
L-Asparagine monohydrate/water	0.005	1.6×10^{28}	284.41	1.70	4.19×10^{25}	10.64	32.35	1.87×10^{22}	11.13	1.07×10^{-9}	8.67×10^{-10}	2.48	3.99×10^{25}	2127	0.9891	24
			292.21	1.64	5.53×10^{25}	10.77		2.69×10^{22}	10.84	1.09×10^{-9}		2.51	5.82×10^{25}	2154		
			299.61	1.49	5.95×10^{25}	8.38		3.75×10^{22}	9.52	1.16×10^{-9}		2.68	6.28×10^{25}	1676		
			302.44	1.59	8.21×10^{25}	9.52		4.23×10^{22}	10.61	1.10×10^{-9}		2.54	8.06×10^{25}	1904		
			312.16	1.35	7.63×10^{25}	5.84		6.32×10^{22}	8.09	1.26×10^{-9}		2.91	7.38×10^{25}	1168		
Dextrose/water	0.0027	1.9×10^{24}	286.42	1.25	3.28×10^{26}	17.01	8.55	5.41×10^{22}	3.99	9.22×10^{-10}	7.57×10^{-10}	2.44	3.31×10^{25}	6124	0.9824	29
			290.45	1.26	3.64×10^{26}	17.03		5.68×10^{22}	4.16	9.03×10^{-10}		2.39	3.49×10^{26}	6131		
			294.52	1.25	3.70×10^{26}	17.07		5.97×10^{22}	4.12	9.07×10^{-10}		2.40	3.67×10^{26}	6144		
			298.60	1.24	3.76×10^{26}	16.55		6.26×10^{22}	4.08	9.12×10^{-10}		2.41	3.73×10^{26}	5958		
			302.46	1.23	3.80×10^{26}	16.36		6.54×10^{22}	4.03	9.18×10^{-10}		2.42	3.86×10^{26}	5889		

Table 1 *(continued)*

API/solvent	R', K s^{-1}	k_n, m^{-3} s^{-1}	T_{nuc}, K	$S = c^*_{nuc}/c^*_{ref}$	Δc_{max}, molecules per m^3	ΔT_{max}, K	ΔG, kJ mol^{-1}	J, m^{-3} s^{-1}	γ, mJ m^{-2}	r_c, m	$V_{cell}^{1/3}$, m	$\lambda = 2r_c/V_{cell}^{1/3}$	N_m/V	t_{ind}, s	r^2	Ref.
Paracetamol/water	0.5	7.2×10^{27}	292.08	1.66	3.16×10^{25}	14.85	21.34	1.09×10^{24}	9.58	9.40×10^{-10}	1.14×10^{-9}	1.64	3.24×10^{26}	30	0.9951	29
			296.03	1.78	4.30×10^{25}	16.99		1.22×10^{24}	10.57	8.95×10^{-10}		1.56	4.16×10^{26}	34		
			304.37	1.49	3.56×10^{25}	11.65		1.55×10^{24}	8.40	1.00×10^{-9}		1.75	3.62×10^{25}	23		
			303.19	1.61	4.29×10^{25}	14.21		1.50×10^{24}	9.47	9.46×10^{-10}		1.65	4.28×10^{25}	28		
			313.66	1.32	3.22×10^{25}	8.12		1.99×10^{24}	6.77	1.12×10^{-9}		1.95	3.24×10^{25}	16		
			318.36	1.28	3.32×10^{25}	7.37		2.25×10^{24}	6.34	1.16×10^{-9}		2.02	3.32×10^{25}	15		
			321.35	1.22	2.80×10^{25}	4.77		2.42×10^{24}	5.48	1.24×10^{-9}		2.17	2.32×10^{25}	10		
Gestodene form1/ethanol	0.0017	1.6×10^{25}	301.58	1.41	2.67×10^{25}	11.43	20.90	3.81×10^{21}	7.49	1.05×10^{-9}	1.20×10^{-9}	1.75	2.62×10^{25}	6857	0.9814	25
			308.32	1.33	2.62×10^{25}	9.71		4.57×10^{21}	6.70	1.11×10^{-9}		1.85	2.67×10^{25}	5829		
			315.44	1.25	2.43×10^{25}	7.62		5.51×10^{21}	5.75	1.20×10^{-9}		2	2.52×10^{25}	4571		
			321.62	1.22	2.59×10^{25}	6.54		6.42×10^{21}	5.43	1.24×10^{-9}		2.06	2.52×10^{25}	3924		
Gestodene form1/ethanol	0.0050	3.4×10^{25}	298.15	1.56	3.31×10^{25}	14.86	19.95	1.09×10^{22}	8.70	9.54×10^{-10}	1.20×10^{-9}	1.59	3.25×10^{25}	2971	0.99	25
			305.02	1.46	3.36×10^{25}	13.02		1.31×10^{22}	7.98	9.96×10^{-10}		1.66	3.41×10^{25}	2603		
			312.40	1.36	3.28×10^{25}	10.67		1.57×10^{22}	7.07	1.06×10^{-9}		1.76	3.37×10^{25}	2133		
			319.46	1.30	3.33×10^{25}	8.70		1.87×10^{22}	6.41	1.11×10^{-9}		1.85	3.26×10^{25}	1740		
Gestodene form1/ethanol	0.0083	2.5×10^{25}	296.18	1.65	3.64×10^{25}	16.83	19.15	1.06×10^{22}	9.27	9.05×10^{-10}	1.20×10^{-9}	1.51	2.15×10^{25}	2019	0.9896	25
			303.62	1.52	3.65×10^{25}	14.41		1.28×10^{22}	8.40	9.51×10^{-10}		1.59	2.23×10^{25}	1730		
			311.76	1.39	3.45×10^{25}	11.30		1.56×10^{22}	7.25	1.02×10^{-9}		1.71	2.13×10^{25}	1356		
			318.83	1.32	3.53×10^{25}	9.33		1.84×10^{22}	6.61	1.07×10^{-9}		1.79	2.07×10^{25}	1120		
Fenofibrate/ethyl acetate	0.0050	3.1×10^{27}	279.80	2.59	1.07×10^{27}	27.37	22.51	1.94×10^{23}	14.43	7.87×10^{-10}	9.92×10^{-10}	1.586	1.07×10^{27}	5474	0.999	31
			284.53	2.54	1.23×10^{27}	27.00		2.28×10^{23}	14.43	7.87×10^{-10}		1.586	1.24×10^{27}	5400		
			287.48	2.52	1.33×10^{27}	26.63		2.52×10^{23}	14.42	7.87×10^{-10}		1.587	1.34×10^{27}	5327		
			290.16	2.49	1.44×10^{27}	26.53		2.75×10^{23}	14.40	7.88×10^{-10}		1.588	1.46×10^{27}	5306		
			292.79	2.47	1.55×10^{27}	26.11		2.99×10^{23}	14.38	7.88×10^{-10}		1.588	1.56×10^{27}	5222		
			295.26	2.45	1.67×10^{27}	25.79		3.24×10^{23}	14.38	7.88×10^{-10}		1.589	1.67×10^{27}	5159		
			296.89	2.43	1.75×10^{27}	25.64		3.40×10^{23}	14.37	7.88×10^{-10}		1.589	1.74×10^{27}	5127		
Vismodegib/MIBK	0.0167	1.5×10^{30}	345.96	2.71	2.74×10^{25}	19.04	51.54	2.48×10^{22}	22.62	9.51×10^{-10}	1.28×10^{-9}	1.49	2.84×10^{25}	1142	0.9975	28
			349.89	2.32	3.92×10^{25}	21.12		3.07×10^{22}	20.35	1.00×10^{-9}		1.57	3.85×10^{25}	1267		
			354.00	2.13	5.08×10^{25}	22.10		3.73×10^{22}	19.10	1.03×10^{-9}		1.62	4.95×10^{25}	1326		
			372.98	3.86	3.24×10^{25}	6.02		9.09×10^{22}	29.14	8.38×10^{-10}		1.31	3.28×10^{25}	361		
			379.98	5.82	2.30×10^{25}	7.98		1.23×10^{23}	35.20	7.62×10^{-10}		1.19	5.92×10^{25}	479		
Carbamazepine–saccharin cocrystal/water	0.0167	9.1×10^{25}	297.27	1.84	7.27×10^{24}	19.17	23.70	6.24×10^{21}	11.39	9.08×10^{-10}	1.57×10^{-9}	1.16	8.34×10^{26}	415	0.9865	32
			298.89	1.80	7.32×10^{24}	18.66		6.57×10^{21}	11.15	9.18×10^{-10}		1.17	9.74×10^{26}	419		
			300.00	1.78	7.42×10^{24}	18.33		6.81×10^{21}	11.03	9.23×10^{-10}		1.18	1.08×10^{27}	411		
			301.23	1.77	7.69×10^{24}	18.27		7.08×10^{21}	11.01	9.24×10^{-10}		1.18	1.15×10^{27}	384		
			302.46	1.76	7.93×10^{24}	18.07		7.36×10^{21}	10.97	9.26×10^{-10}		1.18	1.31×10^{27}	380		
			303.37	1.77	8.26×10^{24}	18.10		7.57×10^{21}	11.03	9.23×10^{-10}		1.18	1.53×10^{27}	376		
			303.85	1.77	8.41×10^{24}	18.10		7.68×10^{21}	11.05	9.22×10^{-10}		1.18	1.73×10^{27}	372		
Ibuprofen/ethanol	0.0167	1.7×10^{30}	287.99	1.58	8.37×10^{26}	6.91	32.75	2.09×10^{24}	10.27	1.12×10^{-9}	1.36×10^{-9}	1.65	7.18×10^{24}	1150	0.9994	26
			291.09	1.59	9.66×10^{26}	6.98		2.32×10^{24}	10.40	1.12×10^{-9}		1.64	7.36×10^{24}	1120		
			293.67	1.58	1.07×10^{27}	6.85		2.62×10^{24}	10.39	1.12×10^{-9}		1.64	7.49×10^{24}	1100		
			296.64	1.56	1.16×10^{27}	6.40		2.99×10^{24}	10.24	1.13×10^{-9}		1.66	7.77×10^{24}	1096		
			299.74	1.55	1.30×10^{27}	6.33		3.43×10^{24}	10.21	1.13×10^{-9}		1.66	7.98×10^{24}	1084		
			303.68	1.54	1.53×10^{27}	6.27		4.07×10^{24}	10.25	1.13×10^{-9}		1.66	8.22×10^{24}	1086		
			306.79	1.53	1.72×10^{27}	6.20		4.65×10^{24}	10.21	1.13×10^{-9}		1.66	8.34×10^{24}	1086		

Table 1 *(continued)*

API/solvent	R', K s^{-1}	k_n, m^{-3} s^{-1}	T_{nuc}, K	$S = c^*_{nuc}/c^*_{ref}$	Δc_{max}, molecules per m^3	ΔT_{max}, K	ΔG, kJ mol^{-1}	J, m^{-3} s^{-1}	γ, mJ m^{-2}	r_c, m	$V_{cell}^{1/3}$, m	$\lambda = 2r_c/V_{cell}^{1/3}$	N_m/V	t_{ind}, s	r^2	Ref.
$NaNO_3$/NaCl–$NaNO_3$–H_2O solution	0.00083	1.7×10^{24}	282.1	1.06	2.24×10^{26}	5.99	9.23	3.29×10^{22}	1.69	1.47×10^{-9}	7.6×10^{-10}	3.89	2.37×10^{26}	7188	0.9226	54
			287.7	1.06	2.39×10^{26}	5.65		3.55×10^{22}	1.71	1.46×10^{-9}		3.87	2.41×10^{26}	6780		
			298.8	1.04	1.96×10^{26}	4.73		4.10×10^{22}	1.40	1.61×10^{-9}		4.27	2.33×10^{26}	5676		
			303.0	1.03	1.55×10^{26}	3.86		4.32×10^{22}	1.17	1.77×10^{-9}		4.67	2.00×10^{26}	4632		
			305.7	1.03	1.32×10^{26}	3.6		4.45×10^{22}	1.04	1.87×10^{-9}		4.96	1.92×10^{26}	4320		
			309.2	1.02	1.24×10^{26}	2.66		4.64×10^{22}	0.97	1.94×10^{-9}		5.13	1.48×10^{26}	3192		
$NaNO_3$/NaCl–$NaNO_3$–H_2O solution	0.001667	2.2×10^{23}	281.06	1.08	2.74×10^{26}	7.06	4.45	3.30×10^{22}	1.52	1.08×10^{-9}	7.6×10^{-10}	2.8	1.40×10^{26}	4236	0.8911	54
			286.9	1.07	2.76×10^{26}	6.39		3.44×10^{22}	1.48	1.09×10^{-9}		2.9	1.32×10^{26}	3834		
			298	1.05	2.42×10^{26}	5.52		3.68×10^{22}	1.27	1.18×10^{-9}		3.1	1.22×10^{26}	3312		
			302.3	1.04	1.96×10^{26}	4.52		3.78×10^{22}	1.08	1.28×10^{-9}		3.4	1.03×10^{26}	2712		
			308.9	1.03	1.45×10^{26}	2.99		3.92×10^{22}	0.85	1.44×10^{-9}		3.8	7.04×10^{25}	1794		
Ammonium oxalate monohydrate/water	0.00083	1.0×10^{29}	299.36	1.40	7.34×10^{25}	1.16	30.07	5.64×10^{23}	8.28	1.20×10^{-9}	6.8×10^{-10}	3.53	7.88×10^{25}	139.7	0.9335	55
			300.45	1.40	7.62×10^{25}	1.00		5.89×10^{23}	8.33	1.20×10^{-9}		3.52	7.09×10^{25}	120.4		
			302.41	1.41	8.23×10^{25}	1.08		6.37×10^{23}	8.47	1.19×10^{-9}		3.49	8.29×10^{25}	130.1		
			306.15	1.40	8.98×10^{25}	0.96		7.37×10^{23}	8.46	1.19×10^{-9}		3.49	8.52×10^{25}	115.6		
			308.75	1.39	9.40×10^{25}	1.00		8.15×10^{23}	8.38	1.19×10^{-9}		3.51	9.82×10^{25}	120.5		
L-Arabinose/water	0.0022	8.7×10^{25}	306.84	1.60	2.15×10^{27}	26.04	15.84	1.76×10^{23}	8.53	8.58×10^{-10}	8.5×10^{-10}	2.01	2.06×10^{27}	11 718	0.9615	56
			311.19	1.61	2.38×10^{27}	28.12		1.92×10^{23}	8.72	8.48×10^{-10}		1.99	2.42×10^{27}	12 654		
			315.54	1.63	2.62×10^{27}	28.68		2.08×10^{23}	8.89	8.40×10^{-10}		1.97	2.69×10^{27}	12 906		
			320.08	1.64	2.89×10^{27}	29.06		2.27×10^{23}	9.06	8.32×10^{-10}		1.96	2.97×10^{27}	13 077		
			325	1.64	3.19×10^{27}	28.68		2.49×10^{23}	9.20	8.26×10^{-10}		1.94	3.21×10^{27}	12 906		
			329.73	1.66	3.55×10^{27}	28.12		2.70×10^{23}	9.41	8.17×10^{-10}		1.92	3.42×10^{27}	12 654		
Cobalt sulfate/water	0.00083	2.3×10^{24}	284.13	1.09	1.32×10^{26}	9.14	12.28	1.30×10^{22}	2.39	1.43×10^{-9}	6.5×10^{-10}	4.39	1.43×10^{26}	10 965	0.9407	15
			290.27	1.10	1.50×10^{26}	7.99		1.45×10^{22}	2.54	1.38×10^{-9}		4.26	1.39×10^{26}	9583		
			296.80	1.08	1.28×10^{26}	6.30		1.63×10^{22}	2.25	1.47×10^{-9}		4.53	1.23×10^{26}	7556		
			310.01	1.04	7.46×10^{25}	3.22		2.01×10^{22}	1.51	1.80×10^{-9}		5.53	7.78×10^{25}	3870		
Cobalt sulfate/water	0.00167	1.5×10^{24}	282.75	1.10	1.50×10^{26}	10.52	9.59	2.56×10^{22}	2.40	1.26×10^{-9}	6.5×10^{-10}	3.87	1.61×10^{26}	6313	0.9399	15
			288.12	1.12	1.80×10^{26}	10.14		2.76×10^{22}	2.64	1.20×10^{-9}		3.69	1.67×10^{26}	6083		
			293.27	1.11	1.80×10^{26}	9.83		2.96×10^{22}	2.60	1.21×10^{-9}		3.73	1.74×10^{26}	5897		
			308.40	1.06	1.01×10^{26}	4.84		3.59×10^{22}	1.70	1.49×10^{-9}		4.60	1.04×10^{26}	2902		
Cobalt sulfate/water	0.0025	9.8×10^{23}	279.83	1.13	1.88×10^{26}	13.44	7.63	3.70×10^{22}	2.58	1.08×10^{-9}	6.5×10^{-10}	3.33	1.99×10^{26}	5375	0.9453	57
			285.05	1.15	2.22×10^{26}	13.21		3.93×10^{22}	2.82	1.04×10^{-9}		3.19	2.08×10^{26}	5283		
			289.20	1.15	2.37×10^{26}	13.90		4.12×10^{22}	2.90	1.02×10^{-9}		3.14	2.29×10^{26}	5559		
			296.72	1.12	1.97×10^{26}	11.52		4.46×10^{22}	2.52	1.10×10^{-9}		3.37	2.06×10^{26}	4607		
			306.78	1.07	1.27×10^{26}	6.45		4.94×10^{22}	1.84	1.28×10^{-9}		3.94	1.27×10^{26}	2580		
Glycine/water	0.00167	2.4×10^{25}	293.86	1.19	3.82×10^{26}	8.94	14.29	7.00×10^{22}	4.11	1.17×10^{-9}	6.9×10^{-10}	3.40	3.76×10^{26}	5365	0.9905	57
			303.32	1.16	3.96×10^{26}	8.06		8.40×10^{22}	3.85	1.21×10^{-9}		3.51	4.06×10^{26}	4833		
			311.52	1.14	4.02×10^{26}	6.87		9.76×10^{22}	3.60	1.25×10^{-9}		3.63	4.02×10^{26}	4123		
			318.61	1.13	4.06×10^{26}	6.06		1.10×10^{23}	3.39	1.29×10^{-9}		3.74	4.01×10^{26}	3636		
Glycine/water	0.005	1.8×10^{25}	290.75	1.26	4.95×10^{26}	12.05	13.54	6.76×10^{22}	4.86	1.05×10^{-9}	6.9×10^{-10}	3.04	1.63×10^{26}	2409	0.9927	57
			300.95	1.22	4.99×10^{26}	10.42		8.17×10^{22}	4.46	1.10×10^{-9}		3.18	1.70×10^{26}	2084		
			309.75	1.18	4.92×10^{26}	8.65		9.53×10^{22}	4.08	1.15×10^{-9}		3.32	1.65×10^{26}	1729		
			316.62	1.17	5.22×10^{26}	8.06		1.07×10^{23}	3.97	1.16×10^{-9}		3.37	1.72×10^{26}	1611		
Na_3VO_4/NaOH solution	0.005	4.6×10^{30}	306.55	1.16	1.23×10^{25}	6.39	49.94	1.44×10^{22}	5.76	1.85×10^{-9}	7.6×10^{-10}	4.88	1.84×10^{25}	1279	0.98	58
			314.08	1.63	6.84×10^{25}	8.98		2.30×10^{22}	13.06	1.23×10^{-9}		3.24	4.13×10^{25}	1795		
			330.52	1.70	1.58×10^{26}	12.42		5.95×10^{22}	14.31	1.18×10^{-9}		3.10	1.48×10^{26}	2484		
			340.55	1.63	2.19×10^{26}	12.79		1.02×10^{23}	13.73	1.20×10^{-9}		3.16	2.60×10^{26}	2557		

Table 1 *(continued)*

API/solvent	R', K s^{-1}	k_n, m^{-3} s^{-1}	T_{nuc}, K	$S = c^*_{nuc}/c^*_{ref}$	Δc_{max}, molecules per m^3	ΔT_{max}, K	ΔG, kJ mol^{-1}	J, m^{-3} s^{-1}	γ, mJ m^{-2}	r_c, m	$V_{cell}^{1/3}$, m	$\lambda = 2r_c/V_{cell}^{1/3}$	N_m/V	t_{ind}, s	r^2	Ref.
Ammonium biborate tetrahydrate/water	0.00083	4.2×10^{25}	283.53	1.21	3.03×10^{25}	9.50	22.72	2.76×10^{21}	5.01	1.34×10^{-9}	3.6×10^{-10}	7.27	3.14×10^{25}	11 396	0.9981	59
			287.85	1.24	4.03×10^{25}	10.14		3.19×10^{21}	5.49	1.28×10^{-9}		6.95	3.88×10^{25}	12 173		
			293.03	1.23	4.56×10^{25}	9.93		3.77×10^{21}	5.36	1.30×10^{-9}		7.03	4.49×10^{25}	11 914		
			306.07	1.15	4.64×10^{25}	6.98		5.61×10^{2}	4.21	1.46×10^{-9}		7.93	4.70×10^{25}	8375		
Ammonium biborate tetrahydrate/water	0.0025	3.4×10^{26}	281.37	1.31	4.08×10^{25}	11.66	24.71	8.86×10^{21}	6.40	1.24×10^{-9}	3.6×10^{-10}	6.71	4.13×10^{25}	4662	0.9988	59
			285.90	1.33	5.14×10^{25}	12.09		1.05×10^{22}	6.75	1.21×10^{-9}		6.53	5.06×10^{25}	4834		
			290.80	1.33	6.08×10^{25}	12.16		1.25×10^{22}	6.81	1.20×10^{-9}		6.50	6.07×10^{25}	4863		
			303.69	1.25	7.18×10^{25}	9.35		1.93×10^{22}	5.92	1.29×10^{-9}		6.98	7.20×10^{25}	3741		
Lysozyme/NaCl solution	0.00028	1.1×10^{34}	300.86	1.82	2.80×10^{23}	9.52	87.15	8.15×10^{18}	17.5	1.41×10^{-9}	7.1×10^{-9}	0.39	2.79×10^{23}	26	0.9952	60
			303.92	2.80	4.12×10^{23}	10.45		1.16×10^{19}	19.4	1.34×10^{-9}		0.37	4.35×10^{23}	29		
			306.43	2.54	7.47×10^{23}	14.15		1.54×10^{19}	23.8	1.21×10^{-9}		0.34	7.82×10^{23}	35		
			307.74	3.13	1.12×10^{24}	17.66		1.78×10^{19}	27.3	1.13×10^{-9}		0.32	1.13×10^{24}	39		
			308.96	3.62	1.15×10^{24}	20.43		2.03×10^{19}	29.6	1.08×10^{-9}		0.30	1.49×10^{24}	42		
$Sr(OH)_2 \cdot 8H_2O$/water	0.00139	1.4×10^{24}	279.65	1.31	2.57×10^{24}	7.37	18.62	4.76×10^{20}	5.81	1.13×10^{-9}	9.8×10^{-10}	2.30	2.52×10^{24}	5306	0.9981	61
			292.96	1.15	2.13×10^{24}	4.39		6.85×10^{20}	3.96	1.37×10^{-9}		2.79	2.16×10^{24}	3161		
			305.02	1.08	1.79×10^{24}	2.76		9.26×10^{20}	2.75	1.64×10^{-9}		3.35	1.84×10^{24}	1987		
			316.88	1.02	7.03×10^{23}	1.06		1.22×10^{21}	1.14	2.54×10^{-9}		5.18	9.30×10^{23}	763		
			327.63	1.01	6.52×10^{23}	0.58		1.54×10^{21}	0.85	2.94×10^{-9}		6.00	6.42×10^{23}	418		
$Sr(OH)_2 \cdot 8H_2O$/water	0.00278	3.5×10^{22}	279.11	1.34	2.81×10^{24}	8.09	8.51	9.90×10^{22}	4.77	8.42×10^{-10}	9.8×10^{-10}	1.72	2.88×10^{26}	2912	0.9802	61
			291.81	1.21	2.77×10^{24}	5.64		1.16×10^{23}	3.67	9.59×10^{-10}		1.96	2.36×10^{26}	2030		
			303.57	1.14	2.87×10^{24}	4.13		1.33×10^{23}	2.94	1.07×10^{-9}		2.19	1.98×10^{26}	1487		
			316.08	1.05	1.71×10^{24}	1.87		1.52×10^{23}	1.61	1.45×10^{-9}		2.96	1.02×10^{26}	673		
			327.28	1.02	1.13×10^{24}	0.84		1.70×10^{23}	0.95	1.88×10^{-9}		3.84	5.14×10^{25}	302		
Zinc lactate/water	0.002775	8.9×10^{24}	300.78	1.30	1.14×10^{25}	11.32	20.16	2.80×10^{21}	6.25	2.27×10^{-9}	1.1×10^{-9}	2.06	1.14×10^{25}	4080.4	0.99832	62
			319.68	1.34	1.97×10^{25}	12.32		4.52×10^{21}	6.88	2.15×10^{-9}		1.96	2.01×10^{25}	4438.7		
			308.81	1.37	1.67×10^{25}	13.29		3.46×10^{21}	7.08	2.12×10^{-9}		1.93	1.66×10^{25}	4789.9		
			329.97	1.40	2.97×10^{25}	14.23		5.72×10^{21}	7.74	2.03×10^{-9}		1.85	2.93×10^{25}	5127.7		
Zinc lactate/water	0.003472	1.1×10^{25}	299.18	1.35	1.29×10^{25}	12.92	19.99	3.46×10^{21}	6.78	2.16×10^{-9}	1.1×10^{-9}	1.97	1.29×10^{25}	3722.2	0.9984	62
			318.00	1.39	2.20×10^{25}	14.00		5.56×10^{21}	7.45	2.06×10^{-9}		1.88	2.24×10^{25}	4032.9		
			307.11	1.42	1.84×10^{25}	14.99		4.25×10^{21}	7.62	2.04×10^{-9}		1.85	1.84×10^{25}	4317.2		
			328.25	1.45	3.26×10^{25}	15.95		7.04×10^{21}	8.30	1.95×10^{-9}		1.78	3.23×10^{25}	4594.0		
Borax/water	0.0033	1.4×10^{27}	278.32	1.65	2.28×10^{25}	10.78	28.07	7.69×10^{21}	9.97	1.06×10^{-9}	1.2×10^{-9}	1.83	2.50×10^{25}	3235	0.9982	63
			282.02	1.62	2.66×10^{25}	10.66		9.03×10^{21}	9.99	1.06×10^{-9}		1.83	2.89×10^{25}	3198		
			288.28	1.48	2.62×10^{25}	8.35		1.17×10^{22}	8.61	1.14×10^{-9}		1.97	2.93×10^{25}	2504		
			292.35	1.43	2.85×10^{25}	7.68		1.38×10^{22}	8.22	1.16×10^{-9}		2.01	3.17×10^{25}	2303		
			295.62	1.41	3.13×10^{25}	7.31		1.56×10^{22}	8.01	1.18×10^{-9}		2.04	3.43×10^{25}	2193		
Borax/water	0.01067	2.3×10^{27}	273.93	2.01	2.93×10^{25}	15.17	26.28	2.22×10^{22}	12.12	9.27×10^{-10}	1.2×10^{-9}	1.60	3.16×10^{24}	1422	0.9967	63
			279.98	1.86	3.21×10^{25}	13.71		2.74×10^{22}	11.47	9.53×10^{-10}		1.65	3.52×10^{25}	1285		
			285.23	1.69	3.35×10^{25}	11.39		3.51×10^{22}	10.29	1.01×10^{-9}		1.74	3.75×10^{25}	1068		
			288.94	1.67	3.83×10^{25}	11.09		4.04×10^{22}	10.19	1.01×10^{-9}		1.75	4.20×10^{25}	1039		
			292.76	1.60	4.10×10^{25}	10.17		4.67×10^{22}	9.71	1.04×10^{-9}		1.79	4.45×10^{25}	954		

Note: the unit cell volumes of all compounds studied were obtained from the crystallographic information files (CIFs) retrieved from the International Centre for Diffraction Data (ICDD) powder diffraction file (PDF-5+, 2025), using the database tools provided by the ICDD.

studied including API/solvent combinations, inorganic compounds, the API intermediate, the amino acid (glycine) and lysozyme. While some systems, such as lysozyme/NaCl, demonstrate a very high coefficient of determination (r^2 = 0.9952), others, like $NaNO_3$/NaCl–H_2O, show relatively lower but still acceptable values (*e.g.*, r^2 = 0.8911 – see Table 1). In crystallisation studies, particularly those relying on thermodynamic or kinetic parameters derived from indirect measurements such as MSZW, an $r^2 \geq 0.9$ is generally considered indicative of a strong model fit. The observed variation in r^2 across different systems does not point to a fundamental limitation of the proposed model but rather reflects statistical constraints inherent to linear regression when applied over narrow MSZW or solubility ranges. Specifically, systems with limited experimental variability, where MSZW data span only a small solubility temperature range are more susceptible to experimental noise, leading to slightly lower r^2 values. This is a well-recognised limitation of linear regression, which benefits from broader data coverage to enhance fit robustness. For example, in the $CoSO_4$/water and $NaNO_3$/NaCl–H_2O systems, ΔT_{max} showed minimal change across the studied solubility concentrations. Moreover, in these systems, ΔT_{max} does not increase consistently with solubility temperature, which disrupts the expected linear trend and leads to greater deviation when the data are transformed and fitted using eqn (7). This inconsistency contributes to higher residuals and reduces the overall r^2 value. Theoretically, nucleation depends on multiple interconnected factors, including the degree of supercooling, nucleation temperature (T_{nuc}), reference solubility temperature (T^*_{ref}), solubility concentration at T^*_{ref} (*i.e.*, c^*_{ref}), supersaturation at the T_{nuc} (*i.e.*, Δc_{max}), and cooling rate. The proposed model performs particularly well in systems where ΔT_{max} increases with solubility temperature, regardless of the applied cooling rate supporting its general applicability across a wide range of crystallisation scenarios.

The ΔG values typically range from 8 to 62 kJ mol^{-1} for the APIs, 13.5 for amino acid, 15.84 kJ mol^{-1} for the API intermediate. The ΔG values for the inorganic compounds range from 4.45 to ~50 kJ mol^{-1}. Most of these values agree with the ΔG values reported for several organic/inorganic compounds.[7,33–51] Furthermore, we also noticed that there doesn't exist a perfect correlation between the molecular weight and the Gibbs free energy of nucleation (see Table 1). However, the ΔG values are higher for compounds with higher molecular weight. Noticeably for the case of the largest molecule studied (lysozyme), eqn (7) predicted a ΔG value of 87 kJ mol^{-1}. This agrees with the classical nucleation theory which states that the higher the molecular volume is tougher in the nucleation. The surface energy, calculated using our model in conjunction with classical nucleation theory, ranges from 0.8517 mJ m^{-2} to 35.2 mJ m^{-2} across all systems studied. The radius of the critical nucleus of all the studied APIs, API intermediate, amino acid and lysozyme was found to be in the range of ~10^{-10} m to ~10^{-9} m. Similar magnitudes were also observed for the inorganic compounds, indicating that the critical nucleus size remains within the nanometre scale across both organic and inorganic solutes. Using the size of the critical radius, we mathematically estimated the number of unit cells constituting the critical nucleus. This was done by calculating the normalized critical nucleus size (λ), defined as the ratio of the diameter of the stable nucleus ($2r_c$) to the cube root of the unit cell volume, V_{cell}. The unit cell volumes for the API crystals were obtained from their respective crystallographic information files (CIF file) (see Table 1). Finally, using this normalized size, the approximate number of unit cells in the critical nucleus was calculated as equal to λ^3. This estimation provides a simple theoretical approximation of the structural size of the critical nucleus in terms of unit cells. Note that, this approach assumes that the spherical critical nucleus has a diameter approximately equal to that of a cube-shaped nucleus composed of unit cells arranged in a simple cubic packing, *i.e.*, the linear dimension of the nucleus is equivalent in both cases. This simplification allows for a geometric approximation of the number of unit cells. While this is a simplification and does not account for molecular packing or anisotropic crystal structures, it provides a first-order estimate of the number of unit cells that compose the critical radius. As shown in Table 1, the estimated diameter of the critical nucleus corresponds to approximately 1–5 times the average linear dimension of a unit cell for all the API–solvent systems studied. For the API–solvent combinations considered, the nucleus is estimated to consist of approximately 1 to 125 unit cells, calculated as λ^3. For inorganic compounds, where λ was found to range from 2 to 8, the critical nucleus is estimated to consist of approximately 8 to 512 unit cells, which is notably larger than the corresponding values estimated for the organic compounds. In the case of small organic molecules such as L-arabinose and glycine (excluding the large biomolecule lysozyme), the critical nucleus was estimated to contain approximately 8 to 64 unit cells, again based on the cube of the corresponding λ values reported in Table 1. In the case of lysozyme, the estimated value of λ suggests that the critical nucleus diameter is approximately equal to the linear dimension of a single unit cell, indicating that the nucleus may be composed of only one unit cell. As previously noted, these estimates are approximate and derived from theoretical calculations, as no direct experimental evidence is currently available to validate these values for the systems studied. Nevertheless, the results show good alignment with prior literature in which similar nucleus sizes (that falls within the range of λ^3 values calculated here) have been reported using both computational simulations and advanced experimental techniques such as *in situ* transmission electron microscopy. For example, Prado *et al.*, used molecular dynamics simulations to estimate the size of the critical nucleus for a model inorganic compound, BaS, and reported similar values.[52] In specific their studies shows that the critical nucleus size typically ranges from 5.9 × 10^{-10} to 6.5 to 10^{-10} m depending on the degree of supercooling. These values

fairly agree with the ones that we obtained for most of the inorganic and organic compounds. Additionally, Nakamura *et al.*, employed *in situ* transmission electron microscopy (TEM) to experimentally observe nucleation from amorphous phases and identified clusters composed of several unit cells forming during early nucleation stages.[53] In specific the TEM results showed experimental evidence of the growth of unit cells containing 24 to 86 unit cells. While their work focused on amorphous-to-crystalline transitions, it provides conceptual support for the cluster sizes estimated in solution-phase crystallisation. In the specific case of lysozyme, which has the largest molecular volume among the systems studied, the calculated ΔG indicates a critical nucleus composed of approximately one unit cell. This observation is consistent with classical nucleation theory, which predicts that systems with large molecular volumes and high interfacial energy require larger energy barriers for nucleation but may only form stable nuclei at very small sizes due to packing constraints and limited supersaturation.

The higher number of unit cells estimated within the critical nucleus of inorganic compounds, compared to organic systems, can be explained by several key factors. First, inorganic crystals typically possess smaller and more symmetrical unit cells, owing to their simpler atomic or ionic structures. In contrast, organic compounds, particularly active pharmaceutical ingredients (APIs), often feature larger and more complex unit cells due to their flexible molecular frameworks and lower packing densities. As a result, for a given critical radius, more inorganic unit cells can be accommodated simply because each unit cell occupies less volume. Second, inorganic compounds tend to exhibit higher interfacial energies (γ), due to the stronger ionic or covalent bonding at the interface between the crystal and the surrounding phase. According to classical nucleation theory, a higher interfacial energy leads to an increased Gibbs free energy barrier and, consequently, a larger critical nucleus radius. When this larger critical radius is compared to the smaller unit cell dimension of an inorganic crystal, the number of unit cells required to form a stable nucleus is further amplified. Finally, the high packing efficiency and structural rigidity of inorganic lattices—featuring uniform, tightly arranged ions or atoms—contrasts with the relative disorder in organic systems, where flexible side chains, hydrogen bonding, and solvent inclusions are more common. This inherent structural order in inorganic systems may favour the formation of larger, more compact nuclei, again increasing the number of unit cells involved in the initial nucleation event.

Finally, we used our model as in eqn (7) to theoretically estimate two more parameters that are important to homogeneous nucleation, this includes in the number density or the number of molecules formed per unit volume, N_m/V when the time is equal to the induction time t_{ind}. According to Kubota, MSZW is assumed to be a point where the accumulated crystals that are grown up to detectable size had reached a fixed value, (N_m/V) when the time $t = t_{ind}$ that can be related to the nucleation rate J by the relation:

$$\frac{N_m}{V} = \int_0^{N_m} d\left(\frac{N}{V}\right) = \int_0^{t_{ind}} J dt = \int_0^{T_{max}} J \frac{d(\Delta T)}{R'} \quad (10)$$

Eqn (2) and eqn (10) can be combined to form:

$$\frac{N_m}{V} = \int_0^{N_m} d\left(\frac{N}{V}\right) = \int_0^{t_{ind}} k_n \cdot \exp(-\Delta G/RT_{nuc}) dt \quad (11)$$

Eqn (10) and (11) can be combined to theoretically calculate the t_{ind} as follows:

$$t_{ind} = \frac{N_m}{V k_n \cdot \exp(-\Delta G/RT_{nuc})} = \frac{N_m}{VJ} \quad (12)$$

where, N_m/V can be obtained from eqn (10) as follows:

$$\frac{N_m}{V} = \frac{J}{R'} \Delta T_{max} \quad (13)$$

Eqn (11) to (13) allows us to theoretically calculate, t_{ind}, and N_m/V for each of the cooling rate provided we have the experimentally obtained information on the MSZW (*i.e.*, ΔT_{max}) and theoretically obtained nucleation rate J (which can be obtained eqn (2) and (7)). From eqn (12) and (13), it can be understood that the induction time is defined as the ratio of the metastable zone width to the cooling rate. In this context, the induction time represents the duration required to observe nucleation at T^*_{nuc} starting from T^*_{ref}. The calculated t_{ind} and N_m/V calculated using eqn (12) and (13) are given in Table 1. Clearly for all the APIs studied, at the MSZW, the N_m/V was found to be equal to 10^{24} to 10^{27} molecules per m^3.

For demonstration purposes, in Fig. 3, we plotted the nucleation rate obtained using the classical nucleation theory as a function of temperature based on the ΔG values calculated using the model proposed as in eqn (7) for all the combinations of solute and solutions involved. It is worth mentioning here that, in this work we considered up to 10 different APIs whose molecular weight ranges from 73.09 to 421.3 g mol^{-1}. For these APIs, according to the model proposed in this work and the nucleation temperature studied, the nucleation rate ranges from 10^{21} to 10^{24} m^{-3} s^{-1}. In Table 1, we showed the theoretically obtained t_{ind} and ΔT_{max} for all the 11 different combinations of API/solvent systems. The N_m/V typically ranges from 10^{24} to 10^{27} molecules per m^3 when time, $t = t_{ind}$. In the case of inorganic compounds, Fig. 3c shows that the nucleation rate (J) ranges from 10^{20} to 10^{23} m^{-3} s^{-1}, with corresponding number densities (N_m/V) between 10^{23} and 10^{26} molecules per m^3. Comparable values were observed for the API intermediate and glycine, where the predicted nucleation rates ranged from 10^{22} to 10^{23} m^{-3} s^{-1}, and the corresponding N_m/V values were between 10^{26} and 10^{27} molecules per m^3. Among all the systems studied, lysozyme, which has the largest molecular volume, exhibited the lowest nucleation rate, on the order of 10^{18} to 10^{19} m^{-3} s^{-1}, with a corresponding number density of 10^{23} to 10^{24} molecules per m^3. According to classical nucleation theory, such low nucleation rates are expected for large molecules, as the Gibbs free energy barrier (ΔG) for

nucleation increases significantly with both molecular volume and interfacial energy. For lysozyme, the calculated ΔG was approximately 87 kJ mol^{-1}, which is substantially higher than the ΔG values estimated for smaller organic molecules in this study. This outcome is consistent with the theoretical prediction that systems with larger molecular volumes or lower supersaturation ratios exhibit higher nucleation barriers and therefore lower nucleation rates.

The theoretical model developed in this work offers a practical and physically grounded framework for extracting key nucleation parameters from metastable zone width (MSZW) data obtained under different cooling rates. Using only three experimentally measurable quantities, MSZW, nucleation temperature, and cooling rate, the model enables the prediction of critical nucleation characteristics, including the nucleation rate kinetic constant, Gibbs free energy of nucleation, induction time, and the number density of nuclei at the onset of crystallisation. A key strength of the model lies in its ability to capture the dependence of nucleation rate on cooling rate, in contrast to existing models (*e.g.*, those by Nývlt, Kubota, and Sangwal), which assume a single, cooling-rate-independent nucleation rate derived from MSZW data. By directly incorporating classical nucleation theory, the proposed model provides a more realistic and adaptable tool for interpreting experimental results under varying process conditions. In addition to kinetic parameters, the model facilitates the estimation of important thermodynamic quantities such as surface free energy, critical nucleus radius, and the approximate number of unit cells constituting the stable nucleus. These estimates are derived by comparing the critical nucleus size to the cube root of unit cell volume, offering valuable molecular-level insight into nucleation behaviour. The model was

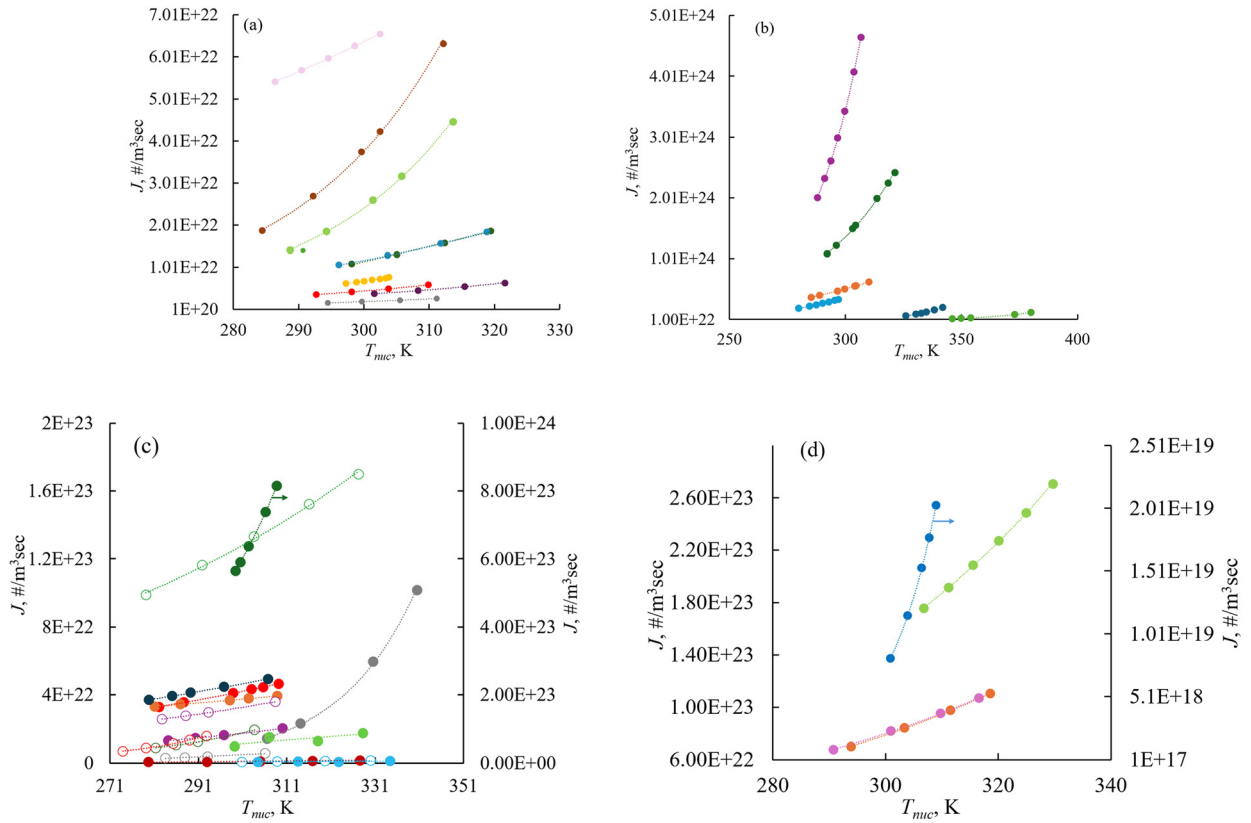

Fig. 3 Plot of nucleation rate *versus* the temperature for (a) 9 combinations of solvents/APIs involving 5 APIs, (b) 6 combinations of solvents/APIs involving 5 APIs, (c) combination of inorganics/solvents involving 8 different compounds and (d) API intermediate, amino acid and a large molecule. Fig. 3a: ●: dextrose/water (R': 0.00278 K s^{-1}); ●: L-asparagine monohydrate/water (R': 0.005 K s^{-1}); ●: L-asparagine monohydrate/water (R': 0.0033 K s^{-1}); ●: gestodene form I/ethanol (R': 0.0083 K s^{-1}); ●: gestodene form I/ethanol (R': 0.005 K s^{-1}); ●: carbamazepine_saccharine/ethanol (R': 0.0167 K s^{-1}); ●: Gestodene form I/ethanol (R': 0.00167 K s^{-1}); ●: pyrazinamide/acetone (R': 0.00167 K s^{-1}); ●: pyrazinamide/acetone (R': 0.0033 K s^{-1}). Fig. 3b: ●: ibuprofen/water (R': 0.0167 K s^{-1}); ●: paracetamol/water (R': 0.5 K s^{-1}); ●: paracetamol/ethanol (R': 0.5 K s^{-1}); ●: fenofibrate/ethyl acetate (R': 0.005 K s^{-1}); ●: psilocybin/water (R': 0.0167 K s^{-1}); ●: vismodegib/MIBK (R': 0.0167 K s^{-1}). Fig. 3c: ●: $NaNO_3$/NaCl + $NaNO_3$ + H_2O solution (R': 0.000833 K s^{-1}); ●: $NaNO_3$/NaCl + $NaNO_3$ + H_2O solution (R': 0.001667 K s^{-1}); ●: $CoSO_4$/water (R': 0.000833 K s^{-1}); ○: $CoSO_4$/water (R': 0.001667 K s^{-1}); ●: $CoSO_4$/water (R': 0.0025 K s^{-1}); ○: $(NH_4)_2B_4O_7{\cdot}4H_2O$/water ($R'$: 0.00833 K s^{-1}); ○: $(NH_4)_2B_4O_7{\cdot}4H_2O$/water ($R'$: 0.0025 K s^{-1}); ●: Na_3VO_4/NaOH solution (R': 0.005 K s^{-1}); ●: $Sr(OH)_2{\cdot}8H_2O$/water (R': 0.001388 K s^{-1}); ○: $Sr(OH)_2{\cdot}8H_2O$/water (R': 0.00277 K s^{-1}); ●: ZnL_2/water (R': 0.00138 K s^{-1}); ○: ZnL_2/water (R': 0.00275 K s^{-1}); ●: borax/water (R': 0.003472 K s^{-1}); ○: borax/water (R': 0.01066 K s^{-1}); ●: ammonium oxalate/water (R': 0.000833 K s^{-1} – plotted in secondary axis). Fig. 3d: ●: L-arabinose/water (R': 0.0083 K s^{-1}); ●: glycine/water (R': 0.001667 K s^{-1}); ●: glycine/water (R': 0.005 K s^{-1}); ●: lysozyme/NaCl solution (R': 0.002778 K s^{-1} – we assumed this cooling rate – shown in secondary axis).

validated using MSZW data from a diverse range of 22 solute–solvent systems, including 11 API–solvent combinations, 8 inorganic compounds, one API intermediate (L-arabinose), one amino acid (glycine), and one biomolecule (lysozyme). In most cases, the model fit the experimental data with coefficients of determination (r^2) exceeding 0.97, confirming its robustness, generality, and predictive accuracy across a wide spectrum of chemical systems.

In terms of theoretical limitations, the model, by design, does not predict the order of nucleation, which is commonly estimated using alternative models such as those developed by Nývlt, Kubota, and Sangwal. As the proposed approach is based on classical nucleation theory, it does not assign a fixed reaction order but rather an Arrhenius-like temperature dependence. While classical nucleation theory predicts a first-order dependence on supersaturation under low-supersaturation conditions, at higher supersaturation, the theory implies a nonlinear and more complex relationship. If needed, an empirical nucleation order can still be inferred using a phenomenological expression such as $J = k'(\Delta c_{max})^n$; where k' is a kinetic constant. In this case, based on the J obtained using eqn (7), the order of nucleation and the kinetic constant, k' according to the power law type expression can be obtained from the linear expression: $\ln J = \ln(k') + n\ln(\Delta c_{max})$. It is worth to mention here that, the primary aim of this work was to develop a model capable of predicting the nucleation rate from MSZW data obtained at different cooling rates. Nucleation fundamentally depends on both supersaturation and induction time, both of which are directly influenced by the cooling rate. This is important because cooling rate is a key process variable that governs the properties of the final crystals. At higher cooling rates, the solution cools rapidly into the labile zone, leading to faster attainment of the critical supersaturation required for nucleation. In such cases, by the time nucleation occurs—after the induction period involving the formation of prenucleation clusters and their structural rearrangement into a stable nucleus—the solution achieves a higher supersaturation. This promotes a higher nucleation rate and results in a larger number of smaller crystals. Conversely, at lower cooling rates, the solution cools more slowly, reaching the induction point at a lower temperature and thus at a lower supersaturation. Here, the longer time allows molecular clusters to form and reorganise at lower driving forces, typically leading to fewer nuclei and larger crystals. This relationship between cooling rate, supersaturation, and nucleation rate is well established, and industries often exploit this by adjusting cooling rates to tailor crystal size and size distribution. In this context, the proposed model is particularly valuable as it can predict nucleation rates as a function of cooling rate. If experimental correlations between MSZW, cooling rate, and solubility are available, the nucleation rate predictions can be linked to the resulting crystal population characteristics. This makes the model useful for designing batch crystallisation processes to achieve targeted product attributes. In continuous crystallisation, knowledge of nucleation rate at different cooling rates is even more critical. The nucleation rate directly determines the production rate (JV) and thus the required residence time to reach a target suspension density or productivity. Higher J values at a given cooling rate reduce the necessary residence time, improving process efficiency. Furthermore, understanding how J varies with cooling rate is essential for designing washout-safe operations, as insufficient nucleation rates relative to dilution rates can lead to washout of nuclei from the crystalliser. Overall, the proposed model is a simple yet useful for analysing nucleation phenomena using MSZW data observed at different cooling rates. Its broad applicability and minimal data requirements make it particularly valuable for both research and industrial crystallisation processes, where understanding and controlling nucleation is essential.

Notation

c^*	Solubility concentration (molecules per m^3) (see eqn (3))
c^*_{nuc}	Solubility concentration at nucleation temperature (molecules per m^3)
c^*_{ref}	Solubility concentration at reference temperature (molecules per m^3)
Δc_{max}	Supersaturation at metastable zone width (molecules per m^3) $\left(= c^*_{ref} - c^*_{nuc}\right)$ (see eqn (5))
ΔG	Critical Gibbs free energy of nucleation (kJ mol^{-1}) (see eqn (1))
J	Nucleation rate (molecules per m^3) (see eqn (2))
k_n	Nucleation rate constant (molecules per m^3 s) (see eqn (1))
$\frac{N_m}{V}$	Number density (molecules per m^3) (see eqn (10))
r_c	Critical radius (m) (see eqn (9))
R	Gas constant, (J mol^{-1} K^{-1}) (see eqn (1))
R'	Cooling rate (K s^{-1}) $\left(= \frac{dT}{dt}\right)$ (see eqn (3))
S	Supersaturation $\left(= c^*_{nuc} - c^*_{ref}\right)$ (dimensionless) (see eqn (8))
t	time (s)
t_{ind}	Induction time (s) (see eqn (12))
T	Solubility temperature (K) (see eqn (3))
T_{nuc}	Nucleation temperature (K) (see eqn (6))
T^*_{ref}	Reference temperature (K)
ΔT_{max}	Metastable zone width (K) $\left(= T^*_{ref} - T^*_{nuc}\right)$ (see eqn (5))
V_{cell}	Unit cell volume (m^3)
γ	Interfacial surface energy (mJ m^{-2}) (see eqn (8))
ϑ	Molecular volume (m^3) (see eqn (8))

Data availability

The ESI† file includes the experimental data, calculation procedures, model equations, and graphical outputs for four representative systems: pyrazinamide, glycine, borax, and lysozyme. Data and calculations for the remaining systems discussed in the manuscript, along with the corresponding

theoretical parameters, are available from the authors upon reasonable request.

Conflicts of interest

There are no conflicts to declare.

Acknowledgements

We acknowledge the financial support of the Science Foundation Ireland (Grant 12/RC/2275, 12/RI/2345/SOF and 18/SIRG/5479). M. V. would like to acknowledge the Bernal Institute, Boston Scientific, Department of Chemical Sciences, and the University of Limerick Foundation for the funding support through the mULtiply program.

References

1 N. Kubota, A New Interpretation of Metastable Zone Widths Measured for Unseeded Solutions, *J. Cryst. Growth*, 2008, **310**, 629–634, DOI: **10.1016/j.jcrysgro.2007.11.123**.
2 K. Sangwal, On the Interpretation of Metastable Zone Width in Anti-Solvent Crystallization, *Cryst. Res. Technol.*, 2010, **45**(9), 909–919, DOI: **10.1002/crat.201000319**.
3 L. D. Shiau, A Linear Regression Model for Determining the Pre-Exponential Factor and Interfacial Energy Based on the Metastable Zone Width Data, *Crystals*, 2020, **10**(2), 103, DOI: **10.3390/cryst10020103**.
4 L. D. Shiau, Comparison of the Nucleation Parameters of Aqueous L-Glycine Solutions in the Presence of l-Arginine from Induction Time and Metastable-Zone-Width Data, *Crystals*, 2021, **11**(10), 1226, DOI: **10.3390/cryst11101226**.
5 *Crystallization*, ed. J. W. Mullin, Butterworth-Heinemann, 4th edn, 2001, ISBN 9780750648332.
6 K. Sangwal, Additives and Crystallization Processes in Industries, in *Additives and Crystallization Processes: From Fundamentals to Applications*, John Wiley & Sons, 2007, ch. 8, pp. 319–379, DOI: **10.1002/9780470517833.CH8**.
7 K. Sangwal, *Nucleation and Crystal Growth: Metastability of Solutions and Melts*, John Wiley & Sons, Inc, 2018.
8 J. Nývlt, Kinetics of Nucleation in Solutions, *J. Cryst. Growth*, 1968, **3–4**, 377–383, DOI: **10.1016/0022-0248(68)90179-6**.
9 K. Sangwal, A Novel Self-Consistent Nývlt-like Equation for Metastable Zone Width Determined by the Polythermal Method, *Cryst. Res. Technol.*, 2009, **44**(3), 231–247, DOI: **10.1002/crat.200800501**.
10 L. D. Shiau, Determination of the Nucleation and Growth Kinetics for Aqueous L-Glycine Solutions from the Turbidity Induction Time Data, *Crystals*, 2018, **8**(11), 403, DOI: **10.3390/cryst8110403**.
11 R. Mohanty, S. Bhandarkar and J. Estrin, Kinetics of Nucleation from Aqueous Solution, *AIChE J.*, 1990, **36**(10), 1536–1544, DOI: **10.1002/aic.690361009**.
12 N. A. Mitchell, P. J. Frawley and C. T. Ó'Ciardhá, Nucleation Kinetics of Paracetamolethanol Solutions from Induction Time Experiments Using Lasentec FBRM®, *J. Cryst. Growth*, 2011, **321**(1), 91–99, DOI: **10.1016/j.jcrysgro.2011.02.027**.
13 J. M. Flannigan, D. MacIver, H. Jolliffe, M. D. Haw and J. Sefcik, Nucleation and Growth Kinetics of Sodium Chloride Crystallization from Water and Deuterium Oxide, *Crystals*, 2023, **13**(9), 1388, DOI: **10.3390/cryst13091388**.
14 S. Maosoongnern and A. E. Flood, Validation of Models Predicting Nucleation Rates from Induction Times and Metastable Zone Widths, *Chem. Eng. Technol.*, 2018, **41**(10), 2066–2076, DOI: **10.1002/ceat.201800313**.
15 J. Zhang and M. Louhi-Kultanen, Determination of Nucleation Kinetics of Cobalt Sulfate by Measuring Metastable Zone Width and Induction Time in Pure and Sulfuric Acid Solution, *Powder Technol.*, 2023, **422**, 118463, DOI: **10.1016/j.powtec.2023.118463**.
16 S. Z. Mohd Noor, D. M. Camacho, C. Yun Ma and T. Mahmud, Effect of Crystallization Conditions on the Metastable Zone Width and Nucleation Kinetics of P-Aminobenzoic Acid in Ethanol, *Chem. Eng. Technol.*, 2020, **43**(6), 1105–1114, DOI: **10.1002/ceat.201900679**.
17 I. D. Tegladza, Q. Liu, G. Lin, J. Zhou, X. Gu and C. Liu, Effect of Trace Sodium Polystyrene Sulfonate on the Solubility, Nucleation and Crystallization of Thiourea from Metastable Zone Width Data, *J. Cryst. Growth*, 2022, **598**, 126869, DOI: **10.1016/j.jcrysgro.2022.126869**.
18 Y. Cao, T. Yao, G. Zhang, Z. Zhou, L. Zhai and S. Wu, Nucleation Behavior of Isosorbide 5-Mononitrate Revealed from Metastable Zone Widths by Combining Nucleation Theory Model and Molecular Simulation, *J. Mol. Liq.*, 2022, **363**, 119846, DOI: **10.1016/j.molliq.2022.119846**.
19 C. Zhao, D. Cao, W. Zhao, S. Xu and Y. Wang, Uncover Cooling Rate and Temperature Dependent on Nucleation Behavior of Nicotinic Acid, *J. Cryst. Growth*, 2021, **568**, 126185, DOI: **10.1016/j.jcrysgro.2021.126185**.
20 G. Wang, Z. Shang, M. Liu, W. Dong, H. Li, H. Yin, J. Gong and S. Wu, Insight into the Nucleation Mechanism of P-Methoxybenzoic Acid in Ethanol-Water System from Metastable Zone Width, *Molecules*, 2022, **27**(13), 4085, DOI: **10.3390/molecules27134085**.
21 M. Ranjbar, M. Vashishtha, G. Walker and K. V. Kumar, Process Analytical Technology Obtained Metastable Zone Width, Nucleation Rate and Solubility of Paracetamol in Isopropanol—Theoretical Analysis, *Pharmaceuticals*, 2025, **18**(3), 314, DOI: **10.3390/PH18030314**.
22 N. A. Mitchell and P. J. Frawley, Nucleation Kinetics of Paracetamolethanol Solutions from Metastable Zone Widths, *J. Cryst. Growth*, 2010, **312**(19), 2740–2746, DOI: **10.1016/j.jcrysgro.2010.05.043**.
23 R. B. Kargbo, A. M. Sherwood, P. Meisenheimer, K. Lenoch and S. Abebe, Psilocybin: Characterization of the Metastable Zone Width (MSZW), Control of Anhydrous Polymorphs, and Particle Size Distribution (PSD), *ACS Omega*, 2022, **7**(6), 5429–5436, DOI: **10.1021/acsomega.1c06708**.
24 M. Lenka and D. Sarkar, Determination of Metastable Zone Width, Induction Period and Primary Nucleation Kinetics for Cooling Crystallization of L-Asparaginenohydrate, *J. Cryst. Growth*, 2014, **408**, 85–90, DOI: **10.1016/j.jcrysgro.2014.09.027**.

25 L. Y. Wang, L. Zhu, L. B. Yang, Y. F. Wang, Z. L. Sha and X. Y. Zhao, Thermodynamic Equilibrium, Metastable Zone Widths, and Nucleation Behavior in the Cooling Crystallization of Gestodene-Ethanol Systems, *J. Cryst. Growth*, 2016, **437**, 32–41, DOI: 10.1016/j.jcrysgro.2015.12.020.

26 A. Rashid, E. T. White, T. Howes, J. D. Litster and I. Marziano, The Metastability and Nucleation Thresholds of Ibuprofen in Ethanol and Water-Ethanol Mixtures, *Int. J. Chem. Eng.*, 2015, **2015**(1), 560930, DOI: 10.1155/2015/560930.

27 M. Parisi, M. Rivallin and A. Chianese, Prediction of Dextrose Nucleation Kinetics by the Growth Rate of Crystallites, *Chem. Eng. Technol.*, 2006, **29**(2), 265–270, DOI: 10.1002/ceat.200500350.

28 R. Angelaud, M. Reynolds, C. Venkatramani, S. Savage, H. Trafelet, T. Landmesser, P. Demel, M. Levis, O. Ruha, B. Rueckert and H. Jaeggi, Manufacturing Development and Genotoxic Impurity Control Strategy of the Hedgehog Pathway Inhibitor Vismodegib, *Org. Process Res. Dev.*, 2016, **20**(8), 1509–1519, DOI: 10.1021/acs.oprd.6b00208.

29 C. J. Brown and X. W. Ni, Determination of Metastable Zone Width, Mean Particle Size and Detectable Number Density Using Video Imaging in an Oscillatory Baffled Crystallizer, *CrystEngComm*, 2012, **14**(8), 2944–2949, DOI: 10.1039/c2ce06628a.

30 A. Maharana and D. Sarkar, Effects of Ultrasound and Its Amplitude on the Metastable Zone Width, Induction Time, and Nucleation Kinetics of Pyrazinamide in Acetone, *Ind. Eng. Chem. Res.*, 2022, **61**(30), 11262–11275, DOI: 10.1021/acs.iecr.2c01123.

31 L. Dwyer, S. Kulkarni, L. Ruelas and A. Myerson, Two-Stage Crystallizer Design for High Loading of Poorly Water-Soluble Pharmaceuticals in Porous Silica Matrices, *Crystals*, 2017, **7**(5), 131, DOI: 10.3390/cryst7050131.

32 K. A. Mohammad, S. Abd Rahim and M. R. Abu Bakar, Kinetics and Nucleation Mechanism of Carbamazepine–Saccharin Co-Crystals in Ethanol Solution, *J. Therm. Anal. Calorim.*, 2017, **130**(3), 1663–1669, DOI: 10.1007/s10973-017-6483-1.

33 H. McTague and Å. C. Rasmuson, Investigation into the Nucleation of the P-Hydroxybenzoic Acid:Glutaric Acid 1:1 Cocrystal from Stoichiometric and Non-Stoichiometric Solutions, *Cryst. Growth Des.*, 2023, **23**(10), 7053–7065, DOI: 10.1021/acs.cgd.2c01522.

34 S. Kakkar, K. R. Devi and Å. C. Rasmuson, Molecular Clustering of Fenoxycarb and Salicylic Acid in Organic Solvents and Relation to Crystal Nucleation, *Cryst. Growth Des.*, 2022, **22**(5), 2824–2836, DOI: 10.1021/ACS.CGD.1C00913/SUPPL_FILE/CG1C00913_SI_001.PDF.

35 J. Zeglinski, M. Kuhs, D. Khamar, A. C. Hegarty, R. K. Devi and Å. C. Rasmuson, Crystal Nucleation of Tolbutamide in Solution: Relationship to Solvent, Solute Conformation, and Solution Structure, *Chem. – Eur. J.*, 2018, **24**(19), 4916–4926, DOI: 10.1002/chem.201705954.

36 J. Liu and Å. C. Rasmuson, Influence of Agitation and Fluid Shear on Primary Nucleation in Solution, *Cryst. Growth Des.*, 2013, **13**(10), 4385–4394, DOI: 10.1021/cg4007636.

37 D. Khamar, J. Zeglinski, D. Mealey and Å. C. Rasmuson, Investigating the Role of Solvent-Solute Interaction in Crystal Nucleation of Salicylic Acid from Organic Solvents, *J. Am. Chem. Soc.*, 2014, **136**(33), 11664–11673, DOI: 10.1021/ja503131w.

38 J. Zeglinski, M. Kuhs, K. R. Devi, D. Khamar, A. C. Hegarty, D. Thompson and Å. C. Rasmuson, Probing Crystal Nucleation of Fenoxycarb from Solution through the Effect of Solvent, *Cryst. Growth Des.*, 2019, **19**(4), 2037–2049, DOI: 10.1021/acs.cgd.8b01387.

39 R. A. Granberg, C. Ducreux, S. Gracin and Å. C. Rasmuson, Primary Nucleation of Paracetamol in Acetone-Water Mixtures, *Chem. Eng. Sci.*, 2001, **56**(7), 2305–2313, DOI: 10.1016/S0009-2509(00)00439-5.

40 O. Pino-García and Å. C. Rasmuson, Primary Nucleation of Vanillin Explored by a Novel Multicell Device, *Ind. Eng. Chem. Res.*, 2003, **42**(20), 4899–4909, DOI: 10.1021/ie0210412.

41 C. Noguera, B. Fritz and A. Clément, Simulation of the Nucleation and Growth of Clay Minerals Coupled with Cation Exchange, *Geochim. Cosmochim. Acta*, 2011, **75**(12), 3402–3418, DOI: 10.1016/j.gca.2011.03.016.

42 A. R. Nielsen, S. Jelavić, D. Murray, B. Rad, M. P. Andersson, M. Ceccato, A. C. Mitchell, S. L. S. Stipp, R. N. Zuckermann and K. K. Sand, Thermodynamic and Kinetic Parameters for Calcite Nucleation on Peptoid and Model Scaffolds: A Step toward Nacre Mimicry, *Cryst. Growth Des.*, 2020, **20**(6), 3762–3771, DOI: 10.1021/acs.cgd.0c00029.

43 L. Shen, H. Sippola, X. Li, D. Lindberg and P. Taskinen, Thermodynamic Modeling of Calcium Sulfate Hydrates in the CaSO4-H2O System from 273.15 to 473.15 K with Extension to 548.15 K, *J. Chem. Eng. Data*, 2019, **64**(6), 2697–2709, DOI: 10.1021/acs.jced.9b00112.

44 T. Hjorth, M. Svärd and Å. C. Rasmuson, Rationalising Crystal Nucleation of Organic Molecules in Solution Using Artificial Neural Networks, *CrystEngComm*, 2019, **21**(3), 449–461, DOI: 10.1039/C8CE01576G.

45 F. L. Nordström, M. Svärd and Å. C. Rasmuson, Primary Nucleation of Salicylamide: The Influence of Process Conditions and Solvent on the Metastable Zone Width, *CrystEngComm*, 2013, **15**(36), 7285–7297, DOI: 10.1039/c3ce40619a.

46 S. Kakkar, K. R. Devi, M. Svärd and Å. Rasmuson, Crystal Nucleation of Salicylamide and a Comparison with Salicylic Acid, *CrystEngComm*, 2020, **22**(19), 3329–3339, DOI: 10.1039/D0CE00168F.

47 D. Mealey, J. Zeglinski, D. Khamar and Å. C. Rasmuson, Influence of Solvent on Crystal Nucleation of Risperidone, *Faraday Discuss.*, 2015, **179**, 309–328, DOI: 10.1039/c4fd00223g.

48 H. McTague and Å. C. Rasmuson, Nucleation of the Theophylline:Salicylic Acid 1:1 Cocrystal, *Cryst. Growth Des.*, 2021, **21**(5), 2711–2719, DOI: 10.1021/acs.cgd.0c01594.

49 C. Heffernan, M. Ukrainczyk, J. Zeglinski, B. K. Hodnett and Å. C. Rasmuson, Influence of Structurally Related Impurities on the Crystal Nucleation of Curcumin, *Cryst. Growth Des.*, 2018, **18**(8), 4715–4723, DOI: 10.1021/acs.cgd.8b00692.

50 H. McTague and Å. C. Rasmuson, Nucleation in the Theophylline/Glutaric Acid Cocrystal System, *Cryst. Growth Des.*, 2021, **21**(7), 3967–3980, DOI: **10.1021/acs.cgd.1c00296**.

51 D. Cheuk, J. Zeglinski, R. Krishnaraj and Å. C. Rasmuson, Influence of Solvent on Crystal Nucleation of Benzocaine, *CrystEngComm*, 2020, **22**(48), 8330–8342, DOI: **10.1039/d0ce01306d**.

52 S. C. C. Prado, J. P. Rino and E. D. Zanotto, Successful Test of the Classical Nucleation Theory by Molecular Dynamic Simulations of BaS, *Comput. Mater. Sci.*, 2019, **161**, 99–106, DOI: **10.1016/j.commatsci.2019.01.023**.

53 T. Nakamuro, M. Sakakibara, H. Nada, K. Harano and E. Nakamura, Capturing the Moment of Emergence of Crystal Nucleus from Disorder, *J. Am. Chem. Soc.*, 2021, **143**(4), 1763–1767, DOI: **10.1021/jacs.0c12100**.

54 C. Bian, H. Chen, X. Song and J. Yu, Metastable Zone Width and the Primary Nucleation Kinetics for Cooling Crystallization of NaNO3 from NaCl-NaNO3-H2O System, *J. Cryst. Growth*, 2019, **518**, 5–13, DOI: **10.1016/j.jcrysgro.2019.04.013**.

55 N. Gherras and G. Fevotte, Comparison between Approaches for the Experimental Determination of Metastable Zone Width: A Case Study of the Batch Cooling Crystallization of Ammonium Oxalate in Water. In, *J. Cryst. Growth*, 2012, **342**(1), 88–98, DOI: **10.1016/j.jcrysgro.2011.06.058**.

56 B. Hu, K. Huang, X. Zhang, P. Zhang and S. Yu, Solubility and Seeded Metastable Zone Width of Functional Sugar L-Arabinose, *Food Sci. Technol.*, 2015, **35**, 51–57, DOI: **10.1590/1678-457X.6329**.

57 J. Bonnin-Paris, B. Stéphane, H. Jean-Louis and H. Fauduet, Determination of the Metastable Zone Width of Glycine Aqueous Solutions for Batch Crystallizations, *Chem. Eng. Commun.*, 2011, **198**(8), 1004–1017, DOI: **10.1080/00986445.2011.545301**.

58 S. Wang, M. Feng, H. Du, J. J. Weigand, Y. Zhang and X. Wang, Determination of Metastable Zone Width, Induction Time and Primary Nucleation Kinetics for Cooling Crystallization of Sodium Orthovanadate from NaOH Solution, *J. Cryst. Growth*, 2020, **545**, 125721, DOI: **10.1016/j.jcrysgro.2020.125721**.

59 O. Sahin, M. Ozdemir, M. S. Izgp, H. Demir and A. A. Ceyhan, Determination of Nucleation Kinetics of Ammonium Biborate Tetrahydrate, *Rev. Chim.*, 2014, **65**, 1462–1466.

60 M. Ildefonso, E. Revalor, P. Punniam, J. B. Salmon, N. Candoni and S. Veesler, Nucleation and Polymorphism Explored via an Easy-to-Use Microfluidic Tool, *J. Cryst. Growth*, 2012, **342**(1), 9–12, DOI: **10.1016/j.jcrysgro.2010.11.098**.

61 X. Zou, S. Liang, Y. Zhang and Y. Wang, Crystallization Thermodynamic Properties and Nucleation Kinetics of Sr(OH)2·8H2O in an Sr(OH)2·8H2O-H2O System, *J. Cryst. Growth*, 2024, **630**, 127589, DOI: **10.1016/j.jcrysgro.2024.127589**.

62 X. Zhang, G. Qian and X. Zhou, Effects of Different Organic Acids on Solubility and Metastable Zone Width of Zinc Lactate, *J. Chem. Eng. Data*, 2012, **57**(11), 2963–2970, DOI: **10.1021/je3006453**.

63 J. Peng, Y. Dong, Z. Nie, F. Kong, Q. Meng and W. Li, Solubility and Metastable Zone Width Measurement of Borax Decahydrate in Potassium Chloride Solution, *J. Chem. Eng. Data*, 2012, **57**(3), 890–895, DOI: **10.1021/je201073e**.

